PHYSICAL REVIEW B **98**, 115149 (2018)

Revealing excitonic processes and chemical bonding in MoS_2 by x-ray spectroscopy

J. C. Woicik,[1] C. Weiland,[1] A. K. Rumaiz,[2] M. Brumbach,[3] N. F. Quackenbush,[1] J. M. Ablett,[4] and E. L. Shirley[5]

[1] *Materials Measurement Science Division, Material Measurement Laboratory,*
National Institute of Standards and Technology, Gaithersburg, Maryland 20899, USA
[2] *National Synchrotron Light Source II, Brookhaven National Laboratory, Upton, New York 11973, USA*
[3] *Materials Characterization Department, Sandia National Laboratories, Albuquerque, New Mexico 87185, USA*
[4] *Synchrotron SOLEIL, L'Orme des Merisiers, Saint-Aubin, BP 48, 91192 Gif-sur-Yvette Cedex, France*
[5] *Sensor Science Division, Physical Measurement Laboratory, National Institute of Standards and Technology,*
Gaithersburg, Maryland 20899, USA

(Received 17 July 2018; revised manuscript received 31 August 2018; published 25 September 2018)

Electron core-hole processes at absorption edges sport several signatures, primarily in the form of bound states and/or excitonic enhancement. Through analysis of the resonant-Raman Auger effect for the two-dimensional transition-metal dichalcogenide MoS_2, we demonstrate that these effects have significant manifestations at the S *K* edge. We characterize two asymmetric excitonically enhanced edges: one at the fundamental band edge and one several electron volts above it following a second band gap that lies entirely within the unoccupied states, with the latter revealing an anomalous postcollision interaction effect. Our interpretation is supported by comparison of both the photoemission valence-band spectrum and the S *K*-edge x-ray-absorption spectrum with electronic structure calculations and an *ab initio* solution of the Bethe-Salpeter equation that accurately accounts for the electron-core-hole interaction.

DOI: 10.1103/PhysRevB.98.115149

I. INTRODUCTION

Since the discovery of its two-hexagonal prismatic structure by Dickinson and Pauling in 1923 [1], the transition-metal dichalcogenide MoS_2 has received significant attention because of its unique optical, electronic, lubricating, photoactive, and catalytic applications [2–6]. Many of the unique properties of this compound stem from its quasi-two-dimensional (2D) crystal structure in addition to its D_{3h} molecular point group that is atypical for sixfold coordinated transition-metal compounds that usually crystallize with octahedral or distorted octahedral symmetry [7]. Recent discovery of a tunable band gap (the bulk or quasi-2D band gap of MoS_2 is 1.29 eV [8]) and the growth of single MoS_2 monolayers [9,10] has stimulated further effort concerning its electronic and optical properties [11–23]. X-ray-absorption near-edge structure (XANES) is a direct experimental probe of the unoccupied density of states of a material; coupled with its intrinsic angular dependence and chemical specificity, it is a powerful method to study chemical bonding in addition to being able to validate calculations of both ground- and excited-state electronic structures.

The goal of our paper is fourfold. First, we present polarization-dependent S *K*-edge XANES data of MoS_2. Second, we explore the electronic structure and electron-core-hole contributions to the XANES via solution of the Bethe-Salpeter equation (BSE) [24]. We find that the S *K* edge consists of two S $1s \rightarrow 3p$ ionization thresholds, with the second edge following a second band gap that lies entirely within the MoS_2 unoccupied states. The fact that the calculations so closely agree with the measured absorption spectra firmly establishes the validity of density functional theory (DFT) and the BSE in predicting the ground- and excited-state electronic structures of MoS_2. It has been stated that an accurate band structure is a prerequisite for an accurate BSE treatment [13], and here we go a step further and prove this *a posteriori* by comparing our DFT densities of states to the high-energy valence-band photoemission spectra of MoS_2. Photoemission is not sensitive to the same core-hole effects as x-ray absorption, and it therefore directly measures a material's ground-state electronic structure more closely. Third, we utilize the resonant-Raman Auger effect to experimentally probe the screening and localization of the x-ray excited states that include the S $1s$ core hole and the photoelectron in the MoS_2 conduction band. The energetics associated with these transitions are consistent with the solution of the BSE for the S *K* edge of MoS_2. Unique to our measurements is the discovery of the postcollision interaction (PCI) Auger effect, i.e., the electronic screening of the core hole by the photoelectron during the Auger decay. Due to its small (or nonexistent) excitonic binding energy, the PCI effect is observed for energies *below* the S $1s \rightarrow 3p$ ionization threshold for the *second* band gap. Lastly, we detail the symmetry aspects of the D_{3h} point group of MoS_2 and explain how it affects both the electronic structure and the polarization dependence of the x-ray-absorption and the valence-photoelectron emission spectra.

II. EXPERIMENTAL

Commercially obtained MoS_2 crystals were mounted on carbon tape and cleaved prior to introduction into the vacuum chamber by the "scotch-tape method" exposing the MoS_2

2469-9950/2018/98(11)/115149(8)

c axis and basal planes. Data were collected at the National Synchrotron Light Source (I and II), Brookhaven National Laboratory, beamlines X24A and SST-2 of the National Institute of Standards and Technology. Additional data were collected at the Galaxies beamline, Synchrotron SOLEIL. XANES spectra were obtained by scanning a Si(111) double-crystal monochromator through the S K edge (~2470-eV photon energy) and recording the sample drain current as a function of photon energy and flux. Auger electron-emission spectra were collected as a function of photon energy around the S K edge by setting the photon energy and scanning the voltage of a hemispherical electron analyzer over the kinetic-energy region of the S K-$L_{2,3}L_{2,3}$ Auger-electron transition (~2116-eV kinetic energy). S $2p$ photoelectron spectra were recorded prior to each Auger measurement to firmly establish the photon energy. Valence-photoemission spectra were recorded with photon energy $h\nu = 2000\,\text{eV}$. All spectra were recorded at near-glancing and near-normal incidence, although we only present the Auger data recorded at near-glancing incidence. For the electron measurements, the cone of the hemispherical electron analyzer was oriented parallel to the polarization vector of the synchrotron x-ray beam and the beam was p polarized.

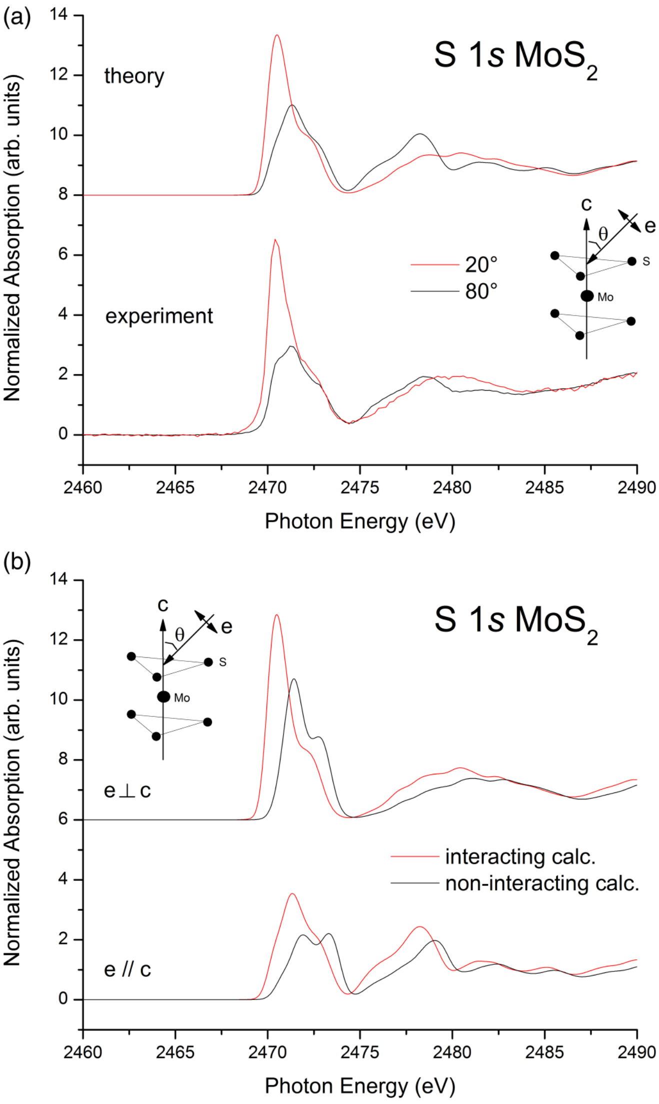

FIG. 1. (a) S K-edge x-ray-absorption near-edge spectra for MoS$_2$. Top: Theory. Bottom: Experiment. (b) Theoretical S K-edge x-ray-absorption near-edge spectra for MoS$_2$ calculated with (top) and without (bottom) the electron-core-hole interaction. The orientation of the polarization vector ***e*** of the synchrotron radiation relative to the MoS$_2$ ***c*** direction is indicated.

III. RESULTS AND DISCUSSION

Figure 1(a) shows the normalized S K-edge XANES spectra recorded with the synchrotron beam aligned at near-glancing (80°) and near-normal (20°) incidence relative to the MoS$_2$ basal planes, as indicated in the inset of the figure. The data have been normalized following standard procedure utilizing the Athena data-analysis software package [25]. They are consistent with those reported in the literature for MoS$_2$ [26,27], but with higher resolution afforded by our use of a Si(111) double-crystal monochromator. Clear from the data is the sharp rise at threshold for the spectra recorded at near-normal incidence and the suppression of the same feature at near-glancing incidence. This transition is attributed to dipole allowed S $1s \rightarrow 3p$ transitions, and it is worth noting that its polarization dependence is directly opposite to what is found for the C $1s$ absorption edge in graphite [28]. There, the first absorption feature is an excitonically enhanced C $1s \rightarrow \pi^*$ transition that has its C $2p$ lobes oriented normal to the plane of the hexagonal C rings, and the second feature is an excitonically enhanced C $1s$ to σ^* transition that has its C hybridized sp^2 lobes oriented within the plane of the rings [29]. Also discernible in our S K-edge spectra is the presence of a second band gap that lies entirely within the unoccupied density of states of MoS$_2$; it exhibits near-zero x-ray absorption beginning at approximately 5 eV above the first x-ray edge. We also note that the turn on of its absorption (the second band edge) has opposite polarization dependence to the first and again it is opposite to what is found for graphite. This observation will be addressed further below.

Figure 1(a) compares the data to theoretical calculations of the S K-edge XANES for MoS$_2$ using the experimental crystal structure [30]. The x-ray near-edge extinction coefficient, $\mu(\varepsilon) = -\text{Im}\langle 0|O^\dagger[\varepsilon + i\gamma(\varepsilon) - H]^{-1}O|0\rangle$, involves the ground state $|0\rangle$, light-matter interaction O, and core-excited Hamiltonian H. H includes electron dynamics (through the band structure), the core-level binding energy, and electron core-hole excitonic effects. We calculated $\mu(\varepsilon)$ using a Bethe-Salpeter treatment [31]. The broadening $\gamma(\varepsilon)$ simulated experimental resolution [the monochromator resolution that was estimated to be 0.22 eV for the Si(111) double-crystal monochromator at the S K edge], electron-damping effects [32], and the core-hole lifetime damping of 0.59 eV [33]. We used norm-conserving pseudopotentials with a Ne-like S core, an [Ar]$3d^{10}$-like Mo core, and a 100-Ry plane-wave cutoff. Following a standard DFT self-consistent-field calculation, we sampled the full Brillouin zone at 20 × 20 × 2 k points, which was well converged, and included 94 conduction bands for six-atom unit cells, which was ample for the spectral region presented. Excellent agreement with experiment is found, with only minor differences of oscillator strengths and energies between the primary features and the signature edge, and it should be emphasized that this agreement has been achieved with no adjustable parameters.

To theoretically determine the excitonic contributions to the absorption spectra, the calculations were repeated, but with the electron-core-hole interaction turned off. Similar procedure has proven effective for determining the electron-core-hole interaction effect in $SrTiO_3$ [34] that possesses O_h symmetry. It is clear from the interacting versus noninteracting calculations shown in Fig. 1(b) that the onsets of both edges, i.e., at the first and at the second band gaps, exhibit significant excitonic enhancement. Considerable redistribution of oscillator strength should always be observed because of the core hole, but it is only in the case of a bound exciton that energy shifts are observed [35], and we note the significant shift of the first but not of the second edge with and without the core-hole interaction included.

To experimentally probe the creation of these excitonically enhanced states, we turn to our resonant S K-$L_{2,3}L_{2,3}$ Auger data. The resonant-Raman Auger effect [36] is a powerful method to study such phenomena, because it is sensitive to the localization and screening of the S $1s$ photoelectron when it is excited into the conduction band. Although originally studied in noble gases [37], it has found significant utility in solid-state physics, having been employed to study excitonic effects in graphite [29] and other crystalline solids [38–41], including MoS_2 [42].

Figure 2 shows the S $^1D_2(K\text{-}L_{2,3}L_{2,3})$ Auger deexcitation spectra for photon energies around the S $1s \rightarrow 3p$ transition. In particular, Fig. 2(a) shows the Auger spectra for photon energies below and increasing up to the maximum of the resonance, whereas Fig. 2(b) shows the Auger spectra for photon energies above it. The resonance energy ($h\nu = 2470.1$ eV) was determined by taking many spectra around the absorption threshold and assigning it to the photon energy that produced the narrowest and most intense resonant peak. Its energy corresponds to the inflection point of the rise of the first edge in Fig. 1(a) (and not to the maximum of absorption); this result indicates that the edge itself has several excitation channels.

Note the classic resonant-Raman shift [36] of the S $^1D_2(K\text{-}L_{2,3}L_{2,3})$ line with photon energy around the S $1s \rightarrow 3p$ transition that confirms the localized nature of the final state achieved by this transition. Around threshold, the Auger peak sharpens, and it disperses linearly with photon energy due to the conservation of energy between the incident photon, the photoelectron in its excited $3p$ excitonic bound state, and the Auger electron in the vacuum. At its maximum intensity and narrowest width, the center of the S $^1D_2(K\text{-}L_{2,3}L_{2,3})$ transition occurs at 2115.8-eV kinetic energy.

To explore more fully the dynamics as the photoelectron transits into the continuum, Fig. 3(a) shows the Auger spectra for a subset of the photon energies studied in Fig. 2(b), but on an expanded energy scale. As the resonant-Raman Auger peak disperses with kinetic energy above the main Auger line, the main or diagram Auger line asymptotically shifts to lower kinetic energy until it reaches its final value of 2115.5 eV. This observation is due to the well-known PCI effect [43] that is classically described by the kinetic-energy gain of the Auger electron as it passes the slowly moving photoelectron. For gases, this effect can be as much as 1 eV, but, due to the greater screening in solids, the effect is reduced by nearly an order of magnitude and consequently often not observed [41].

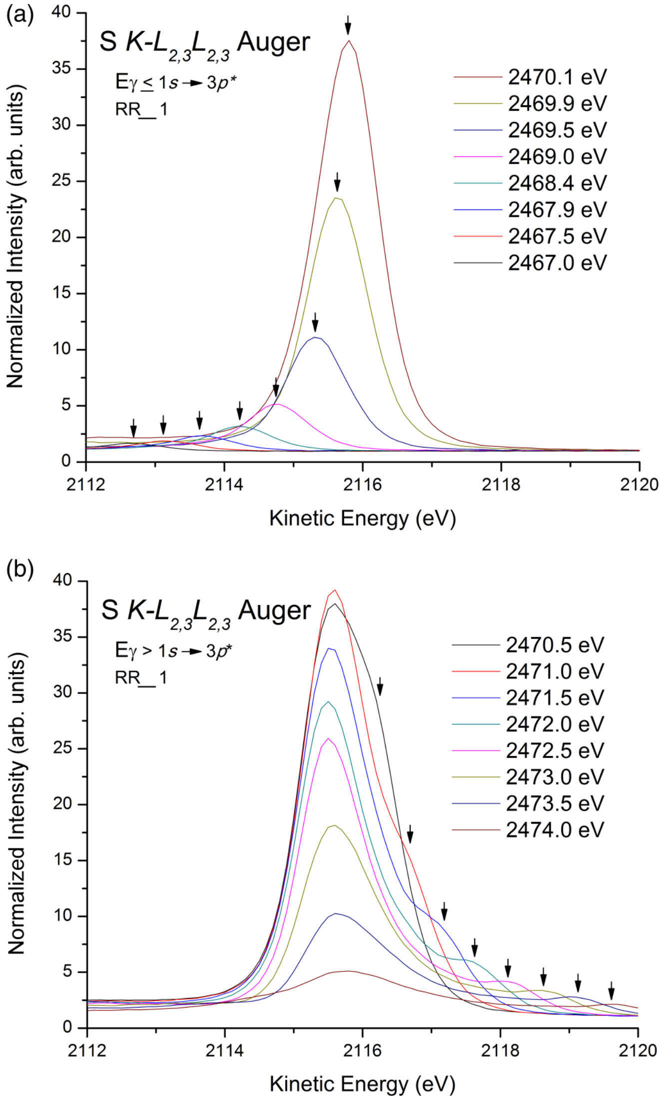

FIG. 2. (a) S $^1D_2(K\text{-}L_{2,3}L_{2,3})$ Auger spectra as a function of photon energy below and up to the first S $1s \rightarrow 3p$ resonance. (b) S $^1D_2(K\text{-}L_{2,3}L_{2,3})$ Auger spectra as a function of photon energy above the first S $1s \rightarrow 3p$ resonance. The resonant-Raman Auger peak, indicated by arrows, may be seen dispersing to higher kinetic energy with increasing photon energy. Note the turn on of the diagram Auger line at 2115.6-eV kinetic energy.

To explore the electron dynamics occurring at the second absorption edge, Fig. 3(b) shows data for a subset of the photon energies studied in Fig. 2(b), but again on an expanded energy scale. A second resonant-Raman Auger peak associated with the second band edge is observed, albeit with a greatly reduced amplitude compared to the first. In fact, the main Auger line and the resonant Auger peak of the first edge are still visible as the second resonant-Raman peak disperses into the main Auger line with increasing photon energy. Also observed is the PCI effect of the second edge, but in this case the main Auger peak shifts to *higher* kinetic energy with increasing photon energy. This unique observation of both *pre*-threshold PCI and *post*-threshold PCI is due to the

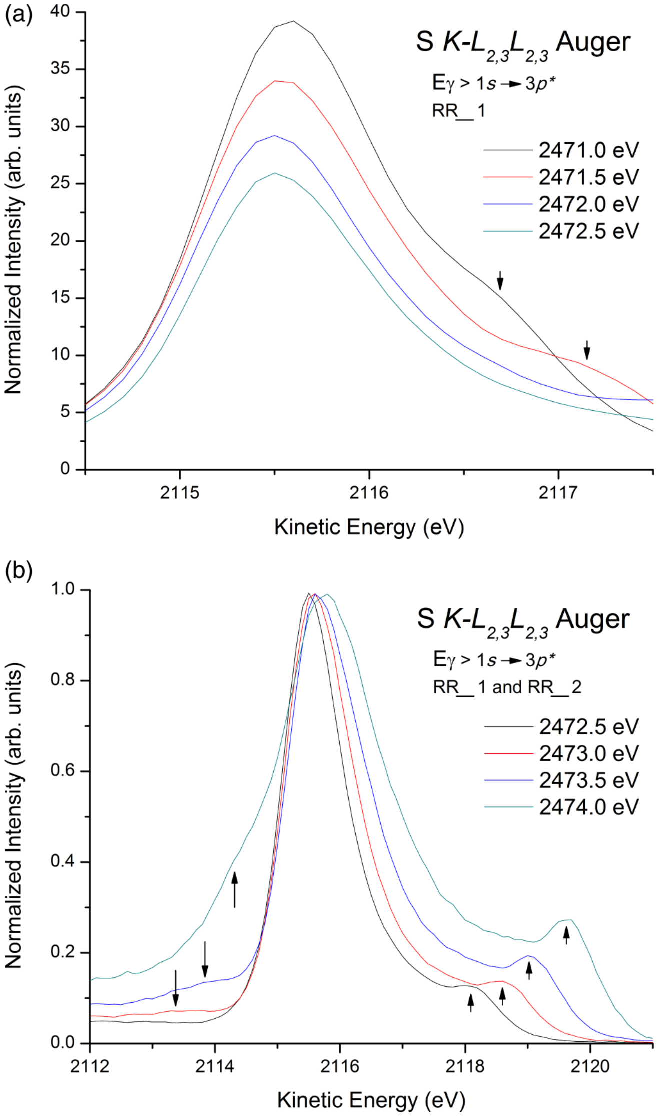

FIG. 3. (a) $\mathrm{S}\,{}^1D_2(K\text{-}L_{2,3}L_{2,3})$ Auger spectra for photon energy above the first S $1s \rightarrow 3p$ resonance. Note the shift of the diagram or main Auger line to *lower* kinetic energy with increasing photon energy illustrating the PCI effect for the first edge. The arrows mark the resonant-Raman Auger peak corresponding to the first S $1s \rightarrow 3p$ resonance. (b) $\mathrm{S}\,{}^1D_2(K\text{-}L_{2,3}L_{2,3})$ Auger spectra for photon energy above the second S $1s \rightarrow 3p$ resonance. Note the shift of the diagram or main Auger line to *higher* kinetic energy with increasing photon energy illustrating the PCI effect for the second edge. The small arrows mark the resonant-Raman Auger peak corresponding to the *first* S $1s \rightarrow 3p$ resonance, and the large arrows mark the resonant-Raman Auger peak corresponding to the *second* S $1s \rightarrow 3p$ resonance. The spectra have been normalized to have equal peak heights.

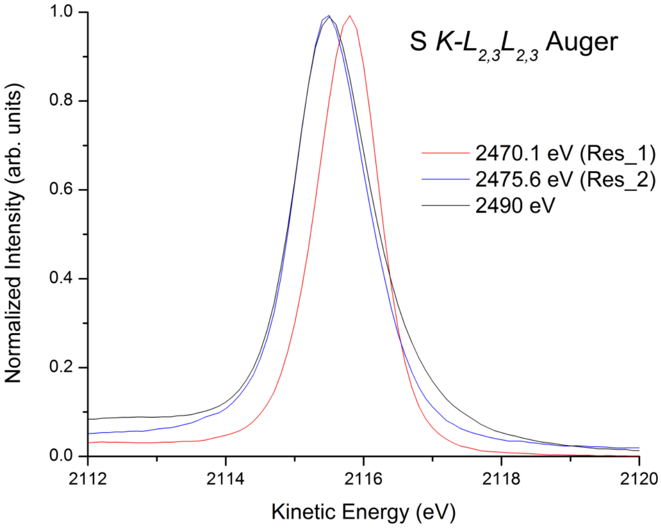

FIG. 4. $\mathrm{S}\,{}^1D_2(K\text{-}L_{2,3}L_{2,3})$ resonant-Raman Auger peak recorded at the resonant photon energies of the first and of the second edges compared to the main or diagram Auger line recorded with photon energy ~20 eV above the first edge. The kinetic-energy shift of the Auger peak at the first resonance is ~0.4 eV, whereas the shift at the second resonance is not measurable (~0 eV). The spectra have been normalized to have equal peak heights.

presence of the second band gap and its reduced excitonic binding energy that is known to scale with the energy of the gap for either two-dimensional or three-dimensional structures [44]. Our data therefore give a full description of the Auger process through the transition region from the photoelectron being in its bound versus continuum final state: The main or diagram Auger line shifts to higher kinetic-energy preresonance, and it shifts back to lower kinetic-energy postresonance.

It may seem surprising that the PCI effect is evident and in fact as strong for the second edge as it is for the first edge, despite its diminished contribution to the x-ray spectra. This result indicates that the magnitude of the PCI effect is not largely affected by either the excitonic binding energy or the amplitude of the resonant-Raman peak. This paradox may be resolved by considering the classical spherical-wave description of the PCI effect as the Auger electron passes the photoelectron. When the Auger electron overtakes the photoelectron at a distance R from the nucleus, the potential (in natural units) felt by the Auger electron changes from $-2e/R$ to $-e/R$, causing an energy shift of the Auger electron by $+e/R$ [45]. Realizing that the PCI effect extends as far as 100 eV above the absorption edge in Ar gas [46], i.e., well above the threshold for the excited photoelectron to be in a bound state, the effect should still be observable even for an excited electron that is only weakly localized on the absorbing atom. We also note that the screened potential of a core hole felt by an electron is reduced by a factor of the dielectric constant at long distances.

To quantify the binding-energy assignments of the first and second edges, Fig. 4 compares the resonant-Raman Auger peaks of the first and second edges recorded at the photon energy of their peak resonances to the Auger peak recorded with the photon energy set ~20 eV above the first resonance. At this relatively high photon energy, the Auger decay is largely decoupled from the initial core ionization, and the energy differences observed give a measure of the excitonic binding energies associated with each edge: $\varepsilon - \varepsilon_A^0 = I_\phi$, which is the energy required to liberate the "excited electron" from the final ionic state [36]. The shift of the resonant-Raman Auger peak of the first edge from the main or normal diagram Auger line is approximately 0.4 eV, whereas no shift is observable at the second edge. These observations are consistent with the BSE solution of Fig. 1 in addition to the excitonic binding energy of 0.44 eV found at the first band edge of MoS_2 by optical valence-band excitations [20]. For comparison, the resonant-Raman shift observed at the Ti K edge of $SrTiO_3$ is ~2 eV [47], and this significantly larger shift is also consistent with the XANES calculations [34]. Note that the band gap of $SrTiO_3$ is much larger than the band gap of MoS_2: 3.2 eV for $SrTiO_3$ [35] and 1.29 eV for MoS_2 [8].

We now turn our attention to the chemical bonding in MoS_2 and our valence-band spectra. In the D_{3h} site symmetry of the Mo ion, the metal $4d$ orbitals can be organized in three sets: the $4d_{3z^2-r^2}$ (A_1' representation), the two partner orbitals $4d_{xy}$ and $4d_{x^2-y^2}$ (E' representation), and the two partner orbitals $4d_{xz}$ and $4d_{yz}$ (E'' representation). We mention these orbitals in order of ascending energy in molecular-orbital theory due to their electrostatic interaction with the doubly anionic S ligands [48]. Simple electron counting gives Mo a formal +4 ionic charge leading to Mo^{4+} $4d^2$ and S^{2-} $3p^6$ configurations.

Figure 5 shows the calculated densities of states centered on both the Mo and S atoms. The densities of states for each have been decomposed according to their group representations, i.e., A_1', E', and E'' on the Mo site, and A_1 and E on the S site, the latter of which we treat in the site symmetry C_{3v} [7]. The reversal of the ordering of the magnitude of the sulfur A_1 and E $3p$ densities of states [Fig. 5(c)] above the first and second band gaps together with the dipole selection rule explains the reversed polarization dependence of the absorption spectrum above the first and second band edges.

It is found that nearly complete mixing of all the ligand and metal states occurs across both the valence and conduction bands. Clearly, this is a solid-state effect due to the long-range periodicity of the crystalline lattice, and it differs significantly from the simplified molecular-orbital description that assigns the top of the valence band to the occupied bonding Mo $4d_{3z^2-r^2}$ orbitals and the bottom of the conduction band to the unoccupied antibonding Mo $4d_{x^2-y^2}$ and $4d_{xy}$ orbitals of the Mo d^2 ion [49,50].

Surprisingly, the calculations also find that there is a relatively small amount of S $3s$-$3p$ contribution to the σ orbitals. However, as stated by Mulliken, a little hybridization goes a long way in stabilizing a chemical bond [51], and one can see from Figs. 5(b) and 5(c) that the contribution from the S $3s$ orbital tracks most closely the contribution from the S $3p_z$ orbital (C_{3v} site symmetry formally allows both sp^2 and p^3 hybridization). We also note that the higher-energy Mo $5s$ orbital accounts for a large fraction of the unoccupied density of states above the second band gap.

Intuitively, the strongest Mo-S bonding should involve a mixture of the S $3p_x$, $3p_y$, and $3p_z$ orbitals that points toward one of the Mo species, because σ bonding is generally much stronger than π bonding. We now consider an S atom in an S plane above the Mo plane, such that its y coordinate is smaller than that of the Mo, but its z coordinate (with the c axis being along the z direction) is larger than that of the Mo. The x coordinates of both atoms are equal. The mixed S $3p$ orbital pointing toward the Mo we designate by $3p'$, and we choose a sign convention so that the lobe of this orbital

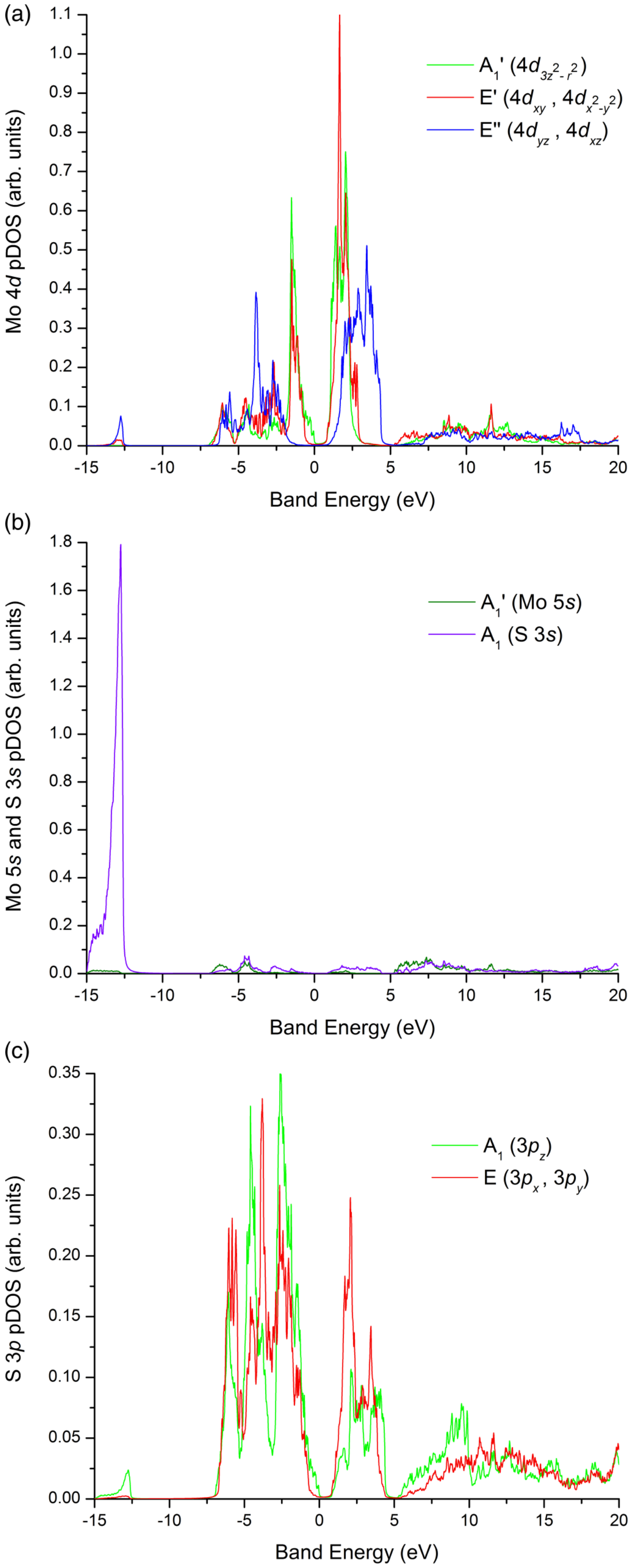

FIG. 5. (a) Mo $4d$ partial densities of states. (b) Mo $5s$ and S $3s$ partial densities of states. (c) S $3p$ partial density of states. When there is more than one group representation in a panel, the symmetries of different orbitals are indicated for the symmetry group of each site.

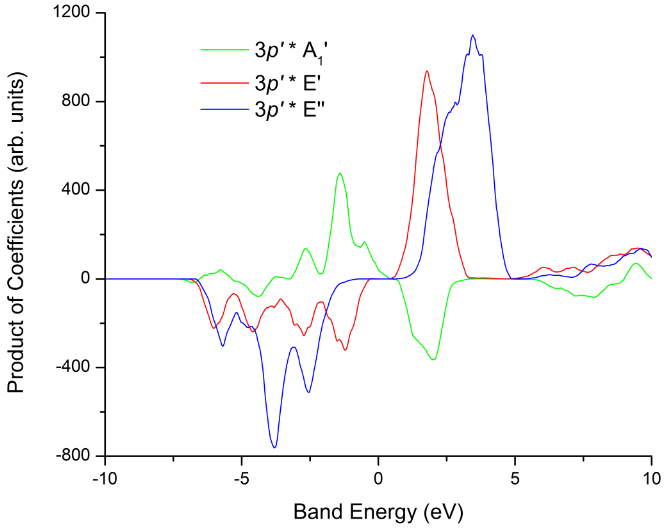

FIG. 6. Boxcar averaged products of the mixing coefficients of the S $3p'$ and neighboring Mo $4d$ orbitals belonging to different representations of the group of the Mo site symmetry.

that is directed toward the Mo is positive. By symmetry, it will not mix significantly in Bloch states with either the E′ Mo $4d_{xy}$ orbital or the E″ Mo $4d_{xz}$ orbital. However, it should mix with the E″ Mo $4d_{yz}$ orbital, preferably with oppositely signed coefficients below the band gap and similarly signed coefficients above the band gap, in an attempt to realize a bonding-antibonding splitting as much as can be achieved on the average for any given bond in a solid. It should also mix with the E′ Mo $4d_{x^2-y^2}$ orbital with analogously signed coefficients above and below the band gap. Finally, the A_1' Mo $4d$ orbital with symmetry that is $3z^2 - r^2 = 2z^2 - x^2 - y^2 = (z^2 - x^2) + (z^2 - y^2)$ will mix with the $3p'$ state presumably as follows: Because the S-Mo bond is about 40° out of the Mo plane, the closeness of this to 45° argues against the $(z^2 - y^2)$ part of the A_1' Mo $4d$ orbital contributing significantly to admixing, whereas the $(z^2 - x^2)$ part has a positive lobe near the S atom that favors admixing with similarly signed coefficients below the band gap and oppositely signed coefficients above the band gap.

In Fig. 6 we present averages over all states of the products of the coefficients of $3p'$ and each of the Mo $4d$ orbitals indicated by its group representation. For this calculation, we used boxcar averaging with a 1-eV-wide window and an $8 \times 8 \times 3$ k-point grid in the full Brillouin zone. It is interesting to find that the A_1', E′, and E″ Mo $4d$ states are mixed with the $3p'$ orbital so that there is an antinode along the bond axis. As already noted above, complete bonding-antibonding cannot be achieved in a crystal because of the periodicity and consequent band structure. On the other hand, the overall signage of the products of the coefficients is completely consistent with our previously stated expectations: The coefficients have either like signs below the band gap and opposite signs above the band gap or *vice versa*.

To further test the validity of our ground-state DFT calculations and their relevance to the MoS$_2$ electronic structure, Fig. 7 shows the valence-band photoelectron spectra recorded at near-glancing (85°) and near-normal incidence (25°) relative to the MoS$_2$ basal planes, as indicated in the inset of the figure. The data have been referenced to the valence-band maximum (VBM), and a Shirley background [52] has been removed. They are consistent with previous report for MoS$_2$ [53], with differences attributable to the photon-energy dependence of the S and Mo photoionization cross sections [54]. The splitting and strong polarization dependence of the valence features further identifies the anisotropic bonding in MoS$_2$. The data are compared to the weighted sums of the partial densities of states shown in Fig. 5 following the description given in Ref. [55], with the exception that the present calculation explicitly considers the angular dependence of the matrix elements [56], while treating lifetime broadening effects in the same way as for the XANES. The agreement between the photoemission data and the calculated spectra directly supports the validity of our ground-state DFT calculation for the electronic structure of MoS$_2$, which itself underpins the BSE calculations of the XANES.

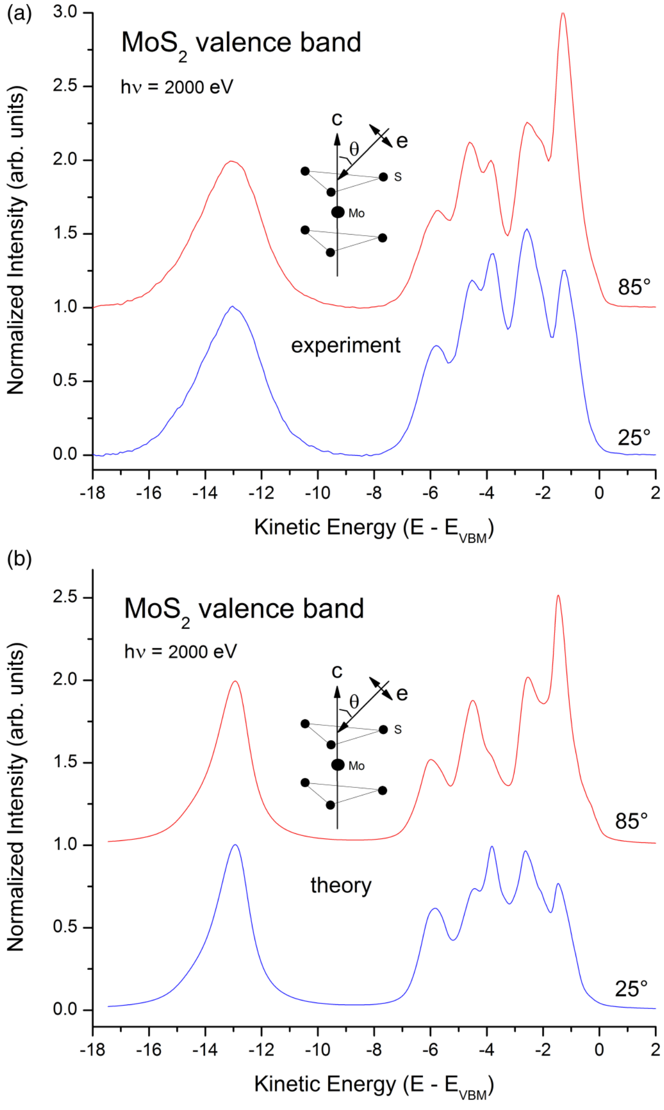

FIG. 7. Valence-band photoemission spectra of MoS$_2$ recorded with photon energy $h\nu = 2000$ eV. (a) Experiment. (b) Theory. The orientation of the polarization vector $\boldsymbol{e}$ of the synchrotron radiation relative to the MoS$_2$ $\boldsymbol{c}$ direction is indicated.

In conclusion, we have studied the S *K*-edge XANES and the photoemission valence band of MoS_2. Agreement is found between calculations utilizing a DFT solution of the ground-state electronic structure followed by solution of the Bethe-Salpeter equation for the excitation spectrum, with the latter being shown to accurately account for the electron-core-hole interaction. Careful analysis of the resonant-Raman Auger effect for this system experimentally confirms the excitonic contributions suggested by the BSE for the two MoS_2 band gaps, the second of which resides completely within the MoS_2 unoccupied density of states. Our calculations of the Mo and S partial densities of states explain the polarization dependence of both the x-ray and photoemission spectra in addition to details of the solid-state chemical bonding between Mo and S such as the nature of the occupied and unoccupied states. Both band edges are found to exhibit postcollision interaction effects, with the second revealing the Coulomb interaction of the Auger electron and the photoelectron below its ionization threshold, i.e., the continuum onset for the electron–two-core-hole final state.

ACKNOWLEDGMENTS

This work was performed at the National Synchrotron Light Source I and II, Brookhaven National Laboratory, beamlines X24A and SST-2 of the National Institute of Standards and Technology. Use of the National Synchrotron Light Source was supported by the US Department of Energy, Office of Basic Energy Sciences, under Contract No. DE-AC02-98CH10886. We also acknowledge SOLEIL for provision of synchrotron radiation facilities (Proposal No. 20170393).

---

[1] R. G. Dickinson and L. Pauling, J. Am. Chem. Soc. **45**, 1466 (1923).

[2] *Physics and Chemistry of Materials with Layered Structures, Optical and Electrical Properties*, edited by P. A. Lee (Reidel, Dordrecht, 1976), Vol. 4.

[3] P. D. Fleischauer, J. R. Lince, P. A. Bertrand, and R. Bauer, Langmuir **5**, 1009 (1989).

[4] J. A. Wilson and A. D. Yoffe, Adv. Phys. **18**, 193 (1969).

[5] M. Daage and R. Chianelli, J. Catal. **149**, 414 (1994).

[6] E. Gourmelon, O. Lignier, H. Hadouda, G. Couturier, J. C. Bernede, J. Tedd, J. Pouzed, and J. Salardenne, Sol. Energy Matter. Sol. Cells **46**, 115 (1997).

[7] F. A. Cotton, *Chemical Applications of Group Theory*, 2nd ed. (Wiley-Interscience, New York, 1971), Chap. 9.

[8] *Gmelin Handbook of Inorganic and Organometallic Chemistry*, 8th ed. (Springer-Verlag, Berlin, 1995), Vol. B7.

[9] A. Splendiani, L. Sun, Y. B. Zhang, T. S. Li, J. Kim, C. Y. Chim, G. Galli, and F. Wang, Nano. Lett. **10**, 1271 (2010).

[10] K. F. Mak, C. Lee, J. Hone, J. Shan, and T. F. Heinz, Phys. Rev. Lett. **105**, 136805 (2010).

[11] S. Lebégue and O. Eriksson, Phys. Rev. B **79**, 115409 (2009).

[12] A. Kuc, N. Zibouche, and T. Heine, Phys. Rev. B **83**, 245213 (2011).

[13] T. Cheiwchanchamnangij and W. R. L. Lambrecht, Phys. Rev. B **85**, 205302 (2012).

[14] H.-P. Komsa and A. V. Krasheninnikov, Phys. Rev. B **86**, 241201(R) (2012).

[15] E. S. Kadantsev and P. Hawrylak, Solid State Commun. **152**, 909 (2012).

[16] A. Kumar and P. K. Ahluwalia, Eur. Phys. J. B **85**, 186 (2012).

[17] A. Kumar and P. K. Ahluwalia, Mater. Chem. Phys. **135**, 755 (2012).

[18] H. Jiang, J. Phys. Chem. C **116**, 7664 (2012).

[19] S. M. Tan, A. Ambrosi, Z. Sofer, Š. Huber, D. Sedmidubský, and M. Pumera, Chem. Eur. J. **21**, 7170 (2015).

[20] H. M. Hill, A. F. Rigosi, C. Roquelet, A. Chernikov, T. C. Berkelbach, D. R. Reichman, M. S. Hybertsen, L. E. Brus, and T. F. Heinz, Nano. Lett. **15**, 2992 (2015).

[21] J. M. Liu, O. Zheliuk, I. Leermakers, N. F. Q. Yuan, U. Zeitler, K. T. Law, and J. T. Ye, Science **350**, 1353 (2015).

[22] D. Costanzo, S. Jo, H. Berger, and A. F. Morpurgo, Nature Nanotech. **11**, 339 (2016).

[23] D. Azhikodan, T. Nautiyal, S. Shallcross, and S. Sharma, Sci. Rep. **6**, 37075 (2016).

[24] E. L. Shirley, Phys. Rev. Lett. **80**, 794 (1998).

[25] B. Ravel and M. Newville, J. Synchrotron Rad. **12**, 537 (2005).

[26] Y. Ohno, K. Hirama, S. Nakai, C. Sugiura, and S. Okada, Phys. Rev. B **27**, 3811 (1983).

[27] D. Li, G. M. Bancroft, M. Kasrai, M. E. Fleet, X. H. Feng, and K. H. Tan, Phys. Chem. Minerals **22**, 123 (1995).

[28] R. A. Rosenberg, P. J. Love, and V. Rehn, Phys. Rev. B **33**, 4034 (1986).

[29] P. A. Brühwiler, A. J. Maxwell, C. Puglia, A. Nilsson, S. Andersson, and N. Mårtensson, Phys. Rev. Lett. **74**, 614 (1995).

[30] P. A. Young, J. Phys. D **1**, 936 (1968).

[31] K. Gilmore, J. Vinson, E. L. Shirley, D. G. Prendergast, C. D. Pemmaraju, J. J. Kas, F. D. Vila, and J. J. Rehr, Comp. Phys. Comm. **197**, 109 (2015); J. Vinson, J. J. Rehr, J. J. Kas, and E. L. Shirley, Phys. Rev. B **83**, 115106 (2011).

[32] T. T. Fister, M. Schmidt, P. Fenter, C. S. Johnson, M. D. Slater, M. K. Y. Chan, and E. L. Shirley, J. Chem. Phys. **135**, 224513 (2011).

[33] M. O. Krause and J. H. Oliver, J. Phys. Chem. Ref. Data **8**, 329 (1979).

[34] T. Yamamoto, T. Mizoguchi, and I. Tanaka, Phys. Rev. B **71**, 245113 (2005).

[35] L. Sponza, V. Véniard, F. Sottile, C. Giorgetti, and L. Reining, Phys. Rev. B **87**, 235102 (2013).

[36] G. B. Armen, H. Aksela, T. Åberg, and S. Aksela, J. Phys. B **33**, R49 (2000).

[37] G. S. Brown, M. H. Chen, B. Crasemann, and G. E. Ice, Phys. Rev. Lett. **45**, 1937 (1980).

[38] H. Wang, J. C. Woicik, T. Åberg, M. H. Chen, A. Herrera-Gomez, T. Kendelewicz, A. Mäntykenttä, K. E. Miyano, S. Southworth, and B. Crasemann, Phys. Rev. A **50**, 1359 (1994).

[39] W. Drube, R. Treusch, and G. Materlik, Phys. Rev. Lett. **74**, 42 (1995).

[40] A. Föhlisch, O. Karis, M. Weinelt, J. Hasselström, A. Nilsson, and N. Mårtensson, Phys. Rev. Lett. **88**, 027601 (2001).

[41] J. Danger, P. Le Fèvre, H. Magnan, D. Chandesris, S. Bourgeois, J. Jupille, T. Eickhoff, and W. Drube, Phys. Rev. Lett. **88**, 243001 (2002).

[42] T. A. Sasaki, Y. Baba, K. Yoshii, and H. Yamamoto, J. Electron Spectrosc. Relat. Phenom. **76**, 411 (1995).

[43] A. Niehaus, J. Phys. B **10**, 1845 (1977).

[44] T. Olsen, S. Latini, F. Rasmussen, and K. S. Thygesen, Phys. Rev. Lett. **116**, 056401 (2016).

[45] J. A. de Gouw, J. van Eck, J. van der Weg, and H. G. M. Heideman, J. Phys. B **28**, 1761 (1995).

[46] R. Guillemin, S. Sheinerman, R. Püttner, T. Marchenko, G. Goldsztejn, L. Journel, R. K. Kushawaha, D. Céolin, M. N. Piancastelli, and M. Simon, Phys. Rev. A **92**, 012503 (2015).

[47] J. C. Woicik, C. Weiland, and A. K. Rumaiz, Phys. Rev. B **91**, 201412(R) (2015).

[48] E. I. Stiefel, R. Eisenberg, R. C. Rosenberg, and H. B. Gray, J. Am. Chem. Soc. **88**, 2956 (1966).

[49] A. Kuc and T. Heine, Chem. Soc. Rev. **44**, 2603 (2015).

[50] N. A. Pike, B. Van Troeye, A. Dewandre, G. Petretto, X. Gonze, G-M. Rignanese, and M. J. Verstraete, Phys. Rev. B **95**, 201106(R) (2017).

[51] C. J. Ballhausen and H. B. Gray, *Molecular Orbital Theory* (Benjamin, New York, 1964), Chap. 4.

[52] D. A. Shirley, Phys. Rev. B **5**, 4709 (1972).

[53] J. R. Lince, S. V. Didziulis, and J. A. Yarmoff, Phys. Rev. B **43**, 4641 (1991).

[54] W. Braun, A. Goldmann, and M. Cardona, Phys. Rev. B **10**, 5069 (1974).

[55] J. C. Woicik, E. J. Nelson, L. Kronik, M. Jain, J. R. Chelikowsky, D. Heskett, L. E. Berman, and G. S. Herman, Phys. Rev. Lett. **89**, 077401 (2002).

[56] E. L. Shirley, L. J. Terminello, J. E. Klepeis, and F. J. Himpsel, Phys. Rev. B **53**, 10296 (1996).